

# Thermal runaway and evaporation of metal nano-tips during intense electron emission

A. Kyritsakis,<sup>1,\*</sup> M. Veske,<sup>1</sup> K. Eimre,<sup>2</sup> V. Zadin,<sup>2</sup> and F. Djurabekova<sup>1</sup>

<sup>1</sup>*Department of Physics and Helsinki Institute of Physics, University of Helsinki,  
PO Box 43 (Pietari Kalmin katu 2), 00014 Helsinki, Finland*

<sup>2</sup>*Intelligent Materials and Systems Lab, Institute of Technology,  
University of Tartu, Nooruse 1, 50411 Tartu, Estonia*

Vacuum arcing (breakdown), is a major limiting factor in various applications such as particle accelerators, fusion reactors etc. Although it is well-known that vacuum arcs appear after intense Field electron Emission (FE), the physical mechanism that leads from FE to the ignition of plasma is not yet well understood. Particle-In-Cell (PIC) simulations have shown that plasma can build up from an intensively emitting Cu cathode, assuming that a high number of neutral atoms are evaporated from it (at least 0.015 Cu atoms per emitted electron). This evaporation rate is impossible to obtain under standard emission conditions and constant emitter shape. However, in this paper we present multi-scale atomistic simulations that reveal a thermal runaway process leading to the evaporation of large parts of the emitter. Our molecular dynamics simulations take into account concurrently and self-consistently various physical processes, namely field-induced forces and deformations, electron emission with finite-size and space-charge effects, Nottingham and Joule heating. We find that fields of realistic values –relevant to high voltage electronic devices– applied on a sufficiently high nano-tip, are able to generate enough heat to partially melt the tip and sufficient force to deform it, elongating and sharpening its apex. This initiates a positive feedback process of heating, sharpening and elongation, which eventually causes evaporation of a large part of the protrusion, in the form of both isolated neutral atoms and charged metal nano-clusters. The obtained mean evaporation rate exceeds the minimum required to ignite plasma as found by previous PIC simulations.

Electric discharges in the form of arcs appearing in vacuum, also known as vacuum breakdowns, have been studied thoroughly for more than 70 years both experimentally and theoretically<sup>1–8</sup>. Vacuum breakdown phenomena play a significant role in various technological applications by being either exploitable or highly undesirable. For example, they can be used to form ion sources<sup>9</sup> and perform physical vapour deposition<sup>7</sup>. On the other hand, they hinder the function and limit the performance of various vacuum devices that require high electric fields, such as fusion reactors<sup>10</sup>, vacuum interrupters<sup>11</sup>, electron sources<sup>4</sup> and especially linear particle accelerators like the compact linear collider (CLIC)<sup>12</sup>.

Although the physical processes that lead to vacuum arcs have been investigated for a long time, their full understanding has not been achieved yet. During an arc, plasma is ignited in the vacuum and burns until the available energy from the power source is consumed. It is well-known since the 1950's<sup>2,3,7,8</sup> that vacuum arcs appear after intense Field electron Emission (FE), but the physical mechanism that leads from FE to the ignition of plasma is not yet fully understood.

One hypothesis commonly used to explain the plasma build-up from an FE process is "explosive emission"<sup>7,13–15</sup>. According to it, when intensive field emission takes place, there is a critical current density beyond which heating is produced at a rate the emitter cannot dissipate. This leads to heat accumulation and extremely high local temperatures, sufficient to cause instant explosion and plasma formation<sup>1,7</sup>. However, this hypothesis is based on only phenomenological considerations, since the atomic level insight in such a complex phenomenon as vacuum arcing was not available.

Here present multiphysics atomistic simulations that reveal a thermal runaway process which is based on the gradual deformation of an emitting tip, due to the field-induced forces. We find that if the current density and tip height are sufficient to partially melt the tip, the field-induced forces gradually deform it, elongating and sharpening its apex in a process similar to the Taylor cone formation in Liquid Metal Ion Sources (LMIS)<sup>16–18</sup>. This process, in combination with the decrease of the electrical and thermal conductivities at high temperatures, leads to a positive feedback thermal runaway mechanism. Eventually large parts of the emitter get evaporated in the form of neutral atoms, but also as charged nano-clusters. The total number of evaporated atoms (both isolated and clustered) is compatible with the minimum evaporation rate required to ignite plasma, as found by recent Particle-In-Cells (PIC) calculations<sup>19,20</sup>.

In order to study the atomic level processes leading to the initiation of plasma, we perform Molecular Dynamics (MD) simulations. However, the thermal runaway process involves various physical phenomena, which classical MD cannot describe implicitly due to the atomistic nature of the method. The electric field interacts with the material, inducing charges and forces on the surface atoms and causing electron emission, which due to the Nottingham<sup>21,22</sup> and Joule effects heats the nano-tip. The combination of these effects causes significant changes in the structure and the geometry of the material and have to be quantified and included in the calculations.

Thus we develop a model, which extends the capability of the MD method by solving the heat and electrostatic equations concurrently for a realistically evolving shape

of the field emitter. We have updated our HELMOD model<sup>23</sup> that couples MD simulations with electric field calculations, and includes the charge-induced forces in the MD interactions. Although this model provided many interesting insights into the interaction of high electric fields with metal surfaces, the rigid grid used to calculate the electric field imposed limitations for systems dynamically evolving under high temperatures. For this we used our recently developed model FEMOCS<sup>24,25</sup> to calculate the electric field distribution around the tip, and combined it with HELMOD to couple the field with MD.

FEMOCS solves the Laplace equation  $\nabla^2\Phi = 0$  using the Finite Element Method (FEM) on an unstructured mesh. This mesh is generated automatically from the atomic positions in order to follow the varying nano-tip shape. A Dirichlet boundary condition  $\Phi = 0$  is then applied on the nano-tip surface. Once the electrostatic potential  $\Phi$  and field  $\vec{E} = -\nabla\Phi$  are obtained, we calculate the induced charge  $Q_s = \epsilon_0|\vec{E}|A_s$  on an elementary surface area  $A_s$  (see supplementary material section I for its definition) of the material-vacuum surface. This surface charge is then distributed to the nearby surface atoms. Given the charge  $q_i$  on each atom, we calculate and add to the MD interaction the Lorentz force  $\vec{F}_i = \frac{1}{2}q_i\vec{E}_i$  and the Coulomb forces between the charged atoms. Details on the implementation of these calculations are given in the supplementary material section I.

Our previous calculations<sup>26,27</sup> showed that the thermal effects caused by electron emission play an important role in the nanotip evolution under high fields. The classical electron emission equations<sup>28-30</sup> are inadequate to describe combined thermal-field emission<sup>31</sup> from nanometrically sharp emitters<sup>32-34</sup>. However, our recently developed computational tool GETELEC<sup>35</sup> provides with the means to consistently and efficiently calculate the electron emission current and Nottingham heat distributions from sharp nano-tips, even at temperatures beyond the melting point. Even so, the local fields and the current densities calculated here are close to the Space Charge (SC) limit; thus the SC effect<sup>36</sup> has to be considered as well.

Calculating fully the charge density distribution induced by the emitted electrons in three dimensions (3D) is a complicated and computationally expensive calculation<sup>37</sup>, which is usually done with the PIC method<sup>38,39</sup>. Nevertheless, Forbes<sup>40</sup> claimed that the standard 1D SC model for field emission<sup>41</sup> can be used to obtain the reduction of the surface field due to the SC if a simple correction is introduced to account for the non-planar nature of the emitter. In order to validate this approximation, we compared the modified 1D SC model to the results of full 3D PIC simulations by Uimanov<sup>39</sup>. We obtain very good agreement with PIC if we modify the 1D model in the following ways: 1)introduce to the 1D space-charge equation representative values for the current density and local field distributions and 2) multiply the applied voltage by a correction factor  $\omega < 1$ .

Details on our SC model can be found in the supplementary material section II.

Using the results from the SC model we calculate the Joule and Nottingham heat distributions along the tip. For the Joule heating, we also need to obtain the resistivity  $\rho$  which depends on the local temperature and the size of the nano-tip. For a given temperature  $T$ , we obtain  $\rho(T)$  by interpolating tabulated values found in the literature<sup>42,43</sup>.  $\rho(T)$  is capped at the highest available value of 3500K, i.e.  $\rho(T \geq 3500\text{K}) = \rho(3500\text{K})$ . Furthermore, the Mean Free Path of the electrons (MFP) in the material is decreased due to the nanometric size of the nano-tip. To correct our  $\rho$  values for this Finite-Size Effect (FSE), we use the simulation method and tool of Yarimbiyik et. al.<sup>44</sup>. The latter can calculate the MFP reduction due to the FSE for a given nanowire diameter. The value we use for the diameter of our tip is the mean diameter along the tip for the initial geometry.

In order to obtain the temperature distribution on the emitter we solve the heat diffusion equation<sup>45</sup>. The geometrical structures we simulate have one dominant dimension, i.e. their height  $h$  is much longer than the lateral dimensions. Hence, in line with our previous publication<sup>26</sup>, we use an 1D version of the heat equation which is solved using an explicit Euler scheme. Thus we obtain the temperature distribution  $T(z, t)$  along the tip for each time step. The heat conductivity  $\kappa$  is calculated from  $\rho$  according to the Wiedemann - Franz law  $\kappa = LT/\rho$ . The Lorentz number  $L$  is known to be reduced for nanometric size structures<sup>46</sup>. Here we used its smallest value  $L = 2.0 \times 10^{-8}\text{W}\Omega\text{K}^{-2}$  reported in<sup>46</sup> for a Cu film of 40nm thickness. A detailed description and validation of the 1D heat diffusion method is given in the supplementary material, section III.

Eventually, the resulting  $T(z)$  is fed back to the calculations for the next step in two ways. First, the current  $T(z)$  is given as input to the electron emission calculations performed by the GETELEC code for the next timestep. Second, it is used to scale the MD atomistic velocities according to the Berendsen<sup>47</sup> temperature control scheme with a relaxation time  $\tau = 1.5\text{ps}$ . The described procedure is repeated for every MD timestep, possibly skipping the full calculation as described in<sup>25</sup>. If the root-mean-square (RMS) average of the atomic displacement (compared to the last full-calculation step) is smaller than 0.38 Å, the last calculated solution is reused.

We simulate a conical Cu nanotip built on a  $\{100\}$  surface (see figure 1). The cone is terminated with a hemispherical cap of a radius  $R = 3\text{nm}$ . The tip has a total height  $h = 93.1\text{nm}$  and a full aperture angle of  $3^\circ$ . In order to keep the computational time feasible, only the upper half of the tip is fully simulated with MD. It is only this part that significantly heats up and its atoms become mobile. The bottom half maintains a practically constant shape and we consider it fixed; the field and temperature calculations extend. Thus the total number of simulated atoms is 206000 and the MD simulation box has a size of  $11.64 \times 11.64 \times 46.6\text{nm}$  (shown with grey lines in figure

1).

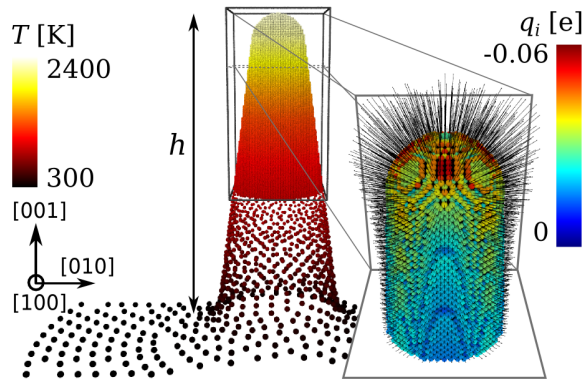


FIG. 1. Simulated tip shape illustrated by the MD atoms (in the box) and the constant "virtual" atoms (out of the box). The color coding represents the steady-state temperature distribution for constant shape. The inset illustrates the atom charges  $q_i$  by the color coding and, the corresponding forces  $\vec{F}_i$  by the black-line arrows.

However the electric field and heat are calculated on the whole tip domain, which includes an extension of the MD system shown by the "virtual" particles lying out of the box in figure 1. These points are used to generate the FEM mesh on a  $280 \times 280 \times 560\text{nm}$  box. This size is sufficient to assume periodic boundary conditions at the sides and a Neumann boundary condition at the top. Note that only a small part of this box is shown in the figure.

For the MD simulations we used two different interatomic potentials with a constant timestep  $\Delta t = 4.05\text{fs}$ . The Sabochick and Lam (SL) EAM potential<sup>48</sup> and the one from Mishin et. al.<sup>49</sup>. For each potential we run repeat the simulation with different seeds in to obtain sufficient statistics. Since our tip is isolated and continued to the bottom, no periodic boundaries were applied. The two bottom layers of the MD systems were fixed in order to account for the connection to the rest of the tip and avoid translational motion of the whole structure. Finally, the ten bottom layers above the two fixed were controlled to linearly increasing temperatures from 0 at the 2nd to  $T(z)$  at the 13th in order to avoid possible artefacts caused by extreme velocity mismatch.

The inset shows a closer view on the tip apex with the color coding corresponding to the calculated field-induced charges  $q_i$  for each atom and the black arrows corresponding to the forces  $\vec{F}_i$ .

A macroscopic electric field  $E_{appl} = 0.8\text{GV/m}$  is applied after the MD system is run to relax for  $0.5\text{ps}$ . At the initial configuration, the maximum local field at the apex as calculated by the Laplace equation is found to be  $E_{max} = 17.9 \pm 0.16\text{GV/m}$ . However, such a high field induces an emitted current density with an average value at the bottom of the MD simulation domain (middle of the conical tip)  $J_{avg} = 3.57 \pm 0.07 \times 10^{-5}\text{Anm}^{-2}$ . This will suppress the fields due to the space-charge ef-

fect by a factor of  $\theta = 0.68 \pm 0.004$  as estimated by our space-charge model, and converge to a final current density of  $J_{avg} = 4.6 \pm 0.06 \times 10^{-6}\text{Anm}^{-2}$ . For the space-charge model, we have assumed an applied voltage of  $V_{appl} = 3\text{kV}$  which is then multiplied by a correction factor  $\omega = 0.25$  in accordance to the calculation explained in section II of the supplementary material.

In this initial configuration, the deposited heat power is very high (reaches  $3 \pm 0.5 \times 10^{-5}\text{Wnm}^{-3}$ ) and is dominated by the Nottingham effect. However, if the system geometry is kept constant, the heat is rapidly dissipated towards the bulk due to the high thermal conductivity of Cu, and the temperature distribution converges to a steady state after about  $233\text{ps}$ , with a maximum value of about  $2370 \pm 30\text{K}$  at the apex. Furthermore, even if the applied field and voltage are increased to unrealistic values (double the previous ones), the current density  $J_{avg}$  is limited by the space charge to a value of  $\approx 1.3 \times 10^{-5}\text{Anm}^{-2}$ , and the maximum steady-state temperature does not exceed  $6200\text{K}$ . All the numerical results reported in the format " $x \pm \delta x$ " correspond to the mean values and standard deviations as obtained from the 32 different simulations we ran.

On the other hand, if we let the whole MD system evolve according to the algorithm described above, we obtain a completely different picture. Figure 2 demonstrates the heat and shape evolution of the nanotip for one of the simulations with the SL potential. The graph shows the time evolution of the height of the tip. The inset figures (a-g) demonstrate the evolution of the tip in the time frames designated on the graph. The tip shape initially stays approximately constant ( $t < 50\text{ps}$ ), while its temperature gradually increases. When the temperature exceeds the melting point at the apex region, the top atoms become mobile and the field-induced forces can pull the apex atoms upwards, thus sharpening and elongating it. This leads to higher local fields, higher forces and higher emission currents, thus producing more heating. The above process increases further the temperature, thus forming a positive feedback loop and eventually leading to thermal runaway.

After about  $200\text{ps}$  the deformed tip has reached more than  $3000\text{K}$  and a slight evaporation rate starts appearing (frame B). Meanwhile, the field-induced forces cause a neck-thinning effect which becomes more intense as the simulation evolves (frame C). This thinning confines the total emitted current in a small cross-sectional area, thus producing a high local current density and Joule heating.

Eventually, the high local temperature in combination with the forces cause detachment of the upper part of the tip, creating an evaporated nano-cluster. The latter is charged (due to partially charged atoms on its surface) and is rapidly accelerated and removed by the field. Although its full behaviour requires further investigation (interaction with the field, collision with the evaporated atoms, emitted electrons, etc), for the purpose of this work we consider it instantly removed and continue the simulation with the remaining tip. All evaporated atoms

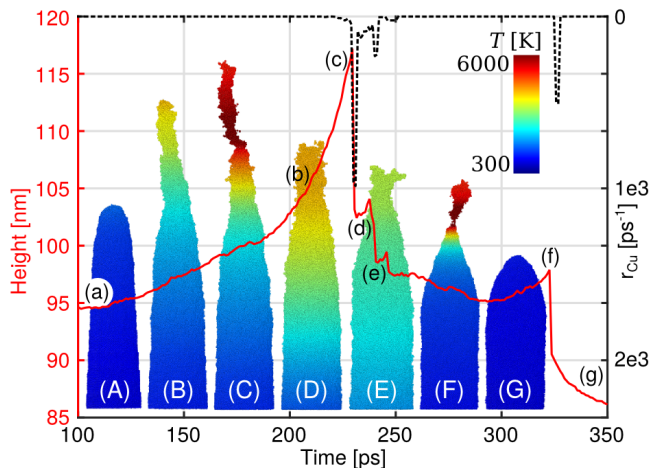


FIG. 2. The tip height (red line, left axis) and the evaporation rate (black dashed line, right axis) as a function of time. The inset images demonstrate the shape and the temperature distribution (color coding) in 7 different frames (A-G). The black lower case letters on the height graph demonstrate the time stamp of each frame (a-g).

and clusters are marked and removed by a cluster analysis algorithm<sup>50</sup> implemented in FEMOCS<sup>25</sup>, with a distance cut-off equal to the one of the MD potential (4.94Å for SL and 5.5Å for Mishin).

The thermal runaway process is reinitialized in the remaining tip until a new smaller cluster is evaporated. After the detachment of several small nanoclusters (frames e,f) and numerous atom evaporation events, the process finally stops as the tip blunts and cools down (frame g). In the various simulations we ran with different random seeds, we found that this process remains qualitatively similar. Although the runaway and the evaporation appears in different times and the tips take various shapes, the steps described above remain qualitatively similar.

An arising question is whether the above process is enough to initiate self-sustaining plasma. In a recent work<sup>19,20</sup>, PIC simulations showed that plasma can build up in the vicinity of an intensively field emitting. This happens if the cathode, in addition to electrons emits neutral Cu atoms at a rate of at least 0.015 neutrals per emitted electron. However, the physical processes that can lead to the emission of neutral metal atoms along with electrons was not fully understood.

We define the average evaporation rate  $\langle r_{Cu} \rangle$  as the total number of atoms detached from the tip (either isolated or clustered) over the total time interval between the first and the last evaporation events. If we divide this quantity by the average emitted electron current during the same period, we obtain the mean evaporation rate per emitted electron  $\langle r_{Cu/e} \rangle = 0.027 \pm 0.015 \text{ atoms/e}$ . This rate is strikingly close to the values assumed in<sup>19</sup> and even exceeds the reported minimum of  $r_{Cu/e} = 0.015 \text{ atoms/e}$  required to ignite plasma. Thus we conclude that this thermal runaway process and the pro-

duced evaporation together can lead to a full vacuum arc.

An important question is what are the prerequisites to initiate the thermal runaway. The latter is a complicated process that depends on various initial configuration parameters, namely material, initial geometry, applied field, anode-cathode distance (affects the space-charge field lowering). A full analysis of all these parameters is out of the scope of this letter, and will be given in a forthcoming publication.

However, a general comment is worthy. There are two main contributing factors to the initiation of the thermal runaway: melting and force. This means that the tip height has to be sufficient to cause temperatures that exceed the melting point at the top. The minimum height depends on various other parameters that affect the heating, namely specific geometry, applied voltage, conductivities. In general, the current density required to produce such a heating is of the order of  $10^{12} \text{ A/m}^2$ , in agreement with the experimental results of Dyke et. al<sup>1,2</sup>. On the other hand, the balance between the field-induced forces and the surface stress plays also a significant role. For the simulations we presented here, a minimum local field at the apex of about 10-12GV/m is necessary. In view of the above, it would be safe to assume that tips with a height of at least several tens of nanometers are required in the case of Cu. This is in agreement with experimental results<sup>51</sup>, demonstrating that field emission with measured enhancement factors of the order 20-100 always precede vacuum arcs on Cu surfaces. This means that assuming a minimum tip radius of 1nm, the involved tips have heights of several tens of nm.

In conclusion, we have simulated the thermal and shape evolution of intensively electron emitting Cu nanotips with an atomistic multiphysics model. Our calculations reveal a thermal runaway process initiated by the field-induced forces acting on the molten apex of a metal nano-tip. The thermal runaway leads to evaporation of metal parts in the form of either atoms or nano-clusters. The evaporation rate exceeds the minimum required to initiate plasma. Thus the presented mechanism can significantly contribute in the initiation of a vacuum arc.

## ACKNOWLEDGEMENTS

The current study was supported by the Academy of Finland project AMELIS, Estonian Research Council Grants PUT 57 and PUT 1372 and the national scholarship program Kristjan Jaak, which is funded and managed by the Archimedes Foundation in collaboration with the Ministry of Education and Research of Estonia. We also acknowledge grants of computer capacity from the Finnish Grid and Cloud Infrastructure (persistent identifier urn:nbn:fi:research-infras-2016072533).

## SUPPLEMENTARY MATERIAL

### I. CALCULATION OF FIELD-INDUCED CHARGES AND FORCES

In order to calculate the charges and forces on the surface atoms, we use an extension of the Molecular Dynamics – ElectroDynamics (MD–ED) method we developed previously for HELMOD<sup>23</sup>. We build a rectangular grid on the Molecular Dynamics (MD) simulation box so that every atom belongs to a certain grid cell. Since the atoms are in an FCC crystal (at least when the temperature is still low), there are numerous grid cells (roughly half) that contain no atoms. Furthermore, when the temperatures approach or exceed the melting point there might be some cells (a small percentage) containing more than one atoms, but this does not affect the functionality of our method.

When each atom is assigned to a certain cell, the cells are separated into material and vacuum domains. Figure 3 illustrates this separation. The cubes correspond to the cells of the material domain, for the initial configuration of the simulated tip after a relaxation of 0.5ps. The maroon spheres correspond to the atomic positions. In the inset a closer view of the area in the box is demonstrated, with the smaller grey cubes corresponding to some of the cells of the vacuum domain.

The separation is done in the following way. If a cell contains an atom or has a number of first nearest neighbours containing an atom  $N \geq 4$ , then it is designated as material (e.g. cell  $c_1$  in the inset). If it does not contain an atom and it has  $N \leq 3$  it is designated as vacuum (e.g. cell  $c_2$  in the inset).

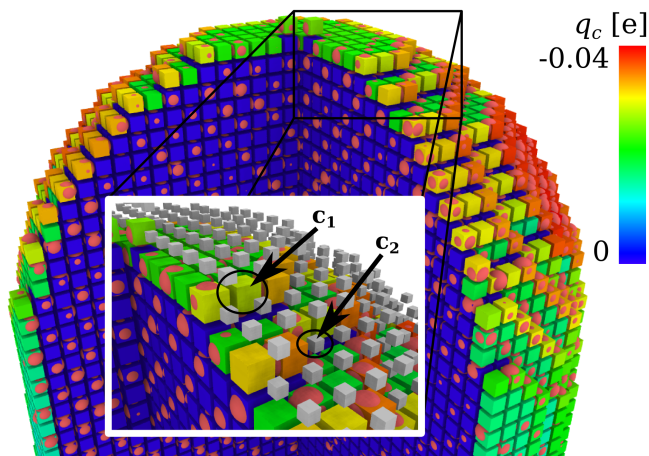


FIG. 3. Atoms on the tip apex (maroon spheres) after a relaxation of 0.5ps along with the corresponding material-designated cubic grid cells. The color coding on the cells corresponds to the charge  $q_c$  assigned to each cell. The inset demonstrates a closer view in the box area, with the grey small cubes being vacuum-designated cells.

Then the surface charges are calculated in every cell

face separating a vacuum cell from a material cell according to the Gauss law

$$q_f = \vec{E}_f \cdot \hat{n}_f A_f \quad (1)$$

where  $q_f$  is the surface charge on each cubic face,  $\vec{E}_f$  is the local electric field in the center of the face, and  $\hat{n}_f$  is the unit vector normal to the cubic surface. The electric field distribution has already been calculated by solving the Laplace equation using the recently developed Finite Element Method (FEM) tool FEMOCS<sup>25</sup>. Then the charge on each surface cubic cell is calculated as

$$q_c = \sum_{f \in MV} q_f \quad (2)$$

where the summation is done over all the faces of the cell that are in contact with a vacuum one. The charges  $q_c$  are shown in the color coding of the cells in figure 3. Note that inner cubic cells that have not a common face with vacuum cells have  $q_c = 0$ .

Since we want to calculate the inter-atomic Coulomb interactions and the field-induced Lorentz forces, the charge on each atom  $q_i$  needs to be calculated. For this, all the grid-point charges have to be assigned to atoms while the total charge is conserved. This is done in a very simple way. If a grid point contains one or more atoms, then all its charge  $q_c$  is assigned to those atoms (divided equally). In the vast majority of the cases there is only one atom in each grid cell. On the other hand, if a grid cell does not contain any atoms, its charge is distributed equally to the atoms belonging to its first-neighbouring cells.

Finally, the Lorentz force  $\vec{F}_i$  on each atom is calculated by the formula  $\vec{F}_i = \frac{1}{2} q_i \vec{E}_i$ . The 1/2 term stands for the fact that the atoms are exposed to the electric field only from the one side of the material-vacuum surface. The Coulomb forces are calculated and included in the MD interaction by the same method described in ref.<sup>23</sup>.

### II. THE 1-DIMENSIONAL SPACE CHARGE MODEL

The space charge (SC) plays an important role in the determination of the electric field and the emission current around the emitter, especially in the very high field regime we simulate here. Although a simple model to describe the SC effects in field emission has been developed since the 1950's<sup>41</sup>, it is applicable only for quasi-planar emitters. Nevertheless, it has been proposed by Forbes<sup>40</sup> that the standard 1D model can be used even for nanometric scale emitters, if the applied voltage  $V$  is multiplied by a correction factor  $\omega < 1$ . Here we describe how this approach is developed, implemented in our simulations, and validated versus existing 3D Particle-In-Cell simulations.

According to the standard 1D SC model, the local field on the emitter (uniform in 1D) is found as  $F = \theta F_L$ ,

where  $\theta$  is the dimensionless field-lowering factor and  $F_L$  is the field found by the Laplace equation, i.e by ignoring the SC effects.  $\theta$  is a function of the the emitted current density  $J$ , the local field  $F$  and the total applied voltage  $V$  which is here an external parameter.  $J$  and  $F$  are also dependent on  $\theta$ , which means that a self-consistent set of  $J, F, \theta$  has to be obtained.

However, for a 3D nanometric emitter,  $J$  and  $F$  are not well-defined. In a quasi-planar emitter, the values at the apex can be used, since the SC is localized around it in a region much smaller than the radius of the emitter, where these quantities are practically constant. On the contrary, in a nanometric emitter the whole tip surface contributes to the SC, which means that the apex values are no longer representative.

Thus we will define the following representative values  $F_r, J_r$  for the field and the current density correspondingly

$$J_r = \frac{\int_{S_h} J dS}{\int_{S_h} dS}$$

$$F_r = \frac{\int_{S_h} F J dS}{\int_{S_h} J dS}. \quad (3)$$

In eq. (3) the surface integrals are performed on the full-width-half-maximum emission surface  $S_h$ , i.e the surface where  $J > \frac{1}{2} J_{max}$ . On this surface,  $J_r$  is the mean value of  $J$  and  $F_r$  is the weighted mean value of  $F$ , with the weight being the emitted current density.

Using the representative values, the  $\theta$  factor is calculated according to equation (13) of reference<sup>40</sup> and then the whole potential and field distributions on the emitter are multiplied by  $\theta$ . Then  $J_r, F_r$  are recalculated according to the new electric field distribution. This procedure is repeated iteratively until self-consistency is reached. Note that the obtained  $\theta$  is used to multiply the whole electric field distribution, thus affecting not only the electron emission, but the charge and forces calculations described in section I.

In order to validate our 1D space charge model, we compare its results to full Particle-In-Cell (PIC) simulations performed by Uimanov<sup>39</sup>. We reproduced the solution of the Laplace equation for the geometries presented in ref.<sup>39</sup>, and then used our model to obtain the field-lowering factor  $\theta$ , using a corrected applied voltage  $\omega V$ .  $\theta$  is obtained for various values of the applied voltage and for two of the geometries simulated by Uimanov: "FE4" and "FE5". "FE4" is an emitter with 10nm radius and "FE5" with 1nm, thus being the most relevant to our simulated tips that have a 3nm radius.

In figure 4 we see the  $F - F_L$  (values at the apex) curves reported in figure 6 of ref.<sup>39</sup> (markers) along with the results of our model (lines) for the same geometries. The corresponding fitted values for the correction factor  $\omega$  are shown in the legends. We see that our model is in very good agreement with the full 3D PIC calculation with an error of less than 1%, at a range of  $F_L$  up to about 35GV/m.

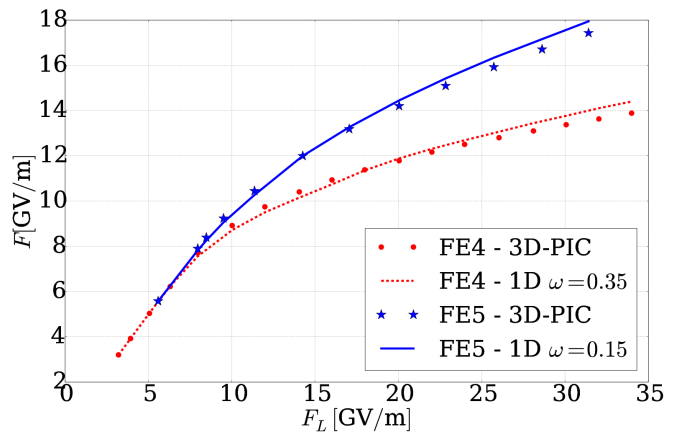


FIG. 4. Local apex field including the SC  $F$  versus the one ignoring SC  $F_L$  for the two different emitter geometries simulated by Uimanov<sup>39</sup>. Markers correspond to the results of figure 6 in ref.<sup>39</sup> and the lines to the results obtained by our 1D SC model.

In view of the above, the 1D space charge model described above is a good approximation for nanometric size emitters, given that a valid correction factor  $\omega$  is used. Although we cannot obtain here its value for the specific geometry we simulate, the fitted values obtained above for similar hemisphere-on-a-cone geometries indicate that the used value  $\omega = 0.25$  is reasonable for our nano-tip. This value was chosen by linearly interpolating between  $\omega = 0.15$  and  $\omega = 0.35$ , with respect to the logarithm of the emitter radii.

### III. SOLUTION OF THE HEAT EQUATION

The heat diffusion equation in 3 dimensions is

$$C_V \frac{\partial T}{\partial t} = \nabla \cdot (\kappa(T) \nabla T) + p \quad (4)$$

where  $C_V$  is the volumetric heat capacity,  $\kappa(T)$  is the heat conductivity as a function of  $T$  and  $p$  is the local deposited volumetric heating power density (in  $\text{W}/\text{m}^3$ ). The Nottingham heat is expressed as surface density (in  $\text{W}/\text{m}^2$ ), but it can also be treated as a volumetric quantity, localized in the surface region with the help of the Dirac  $\delta$  function. In the following analysis it is considered to be a component of the volumetric density  $p$ .

Since the length of the simulated structures is dominant, let us integrate the temperature  $T(x, y, z)$  on an infinitesimal "slice"  $\Omega$ , between  $z$  and  $z + \delta z$  with width  $\delta z$ , cross-sectional area  $A(z)$  and volume  $\delta V = A(z) \delta z$

$$C_V \frac{\partial}{\partial t} \int_{\Omega} T dV = \int_{\Omega} \nabla \cdot (\kappa \nabla T) dV + \int_{\Omega} p dV. \quad (5)$$

The integral of the left hand side equals to  $\langle T \rangle \delta V$  where  $\langle T \rangle$  denotes the mean temperature on  $\Omega$ . The second term in the right hand side equals to the total heat

$\langle p \rangle \delta V$  deposited on the slice. Using the above notation and Gauss's divergence theorem we can rewrite eq. (5) as

$$C_V \frac{\partial \langle T \rangle}{\partial t} \delta V = \oint_{\partial \Omega} \kappa (\nabla T) \cdot \hat{n} dS + \langle p \rangle \delta V. \quad (6)$$

where  $\hat{n}$  denotes the unit vector perpendicular to the surface around the slice  $\partial \Omega$ . This surface has three components. The two cross-sections  $A(z)$  and  $A(z + \delta z)$  and the ring around them. For  $\delta z \ll 1$  the contribution of the ring is negligible compared to  $A$ . Moreover, since the cross-sectional surfaces are along the  $x-y$  plane, we have  $\hat{n} \cdot \nabla T = \partial T / \partial z$  and the surface integral on the cross-section can be expressed as  $A(z) \partial \langle T \rangle / \partial z$ . Then eq. (6) yields

$$C_V \frac{\partial \langle T \rangle}{\partial t} A(z) \delta z = A(z + \delta z) \kappa(z + \delta z) \left. \frac{\partial \langle T \rangle}{\partial z} \right|_{z + \delta z} - A(z) \kappa(z) \left. \frac{\partial \langle T \rangle}{\partial z} \right|_z + \langle p \rangle A(z) \delta z. \quad (7)$$

Dividing eq. (7) by  $A(z) \delta z$  and considering that the temperature does not vary significantly in the lateral directions, i.e.  $\langle T \rangle \approx T$ , yields the 1-dimensional (1D) heat equation for a variable cross-section and conductivity wire.

$$C_V \frac{\partial T}{\partial t} = \frac{1}{A} \frac{\partial}{\partial z} \left[ A \kappa \frac{\partial T}{\partial z} \right] + \langle p \rangle. \quad (8)$$

The above equation is solved using the Finite Difference Method (FDM) with a simple explicit Euler scheme and a small time step  $\Delta t = 0.06$ fs, small enough to avoid numerical instabilities. We divide the tip in  $N$  finite slices with width  $\Delta z$ , that coincide with the slices of the rectangular grid shown in figure 3. On each surface cell the current density and the deposited Nottingham heat surface density are calculated by GETELEC, as described in ref.<sup>35</sup> (the space charge is also taken into account as described in section II). Then the total current and total Nottingham heating power contributions of each cell ( $i_c$  and  $p_{N_c}$  correspondingly) are calculated by multiplying the densities with the cell face areas, similarly to the charge calculation described by equations (1), (2) in the previous section. We consider that the emission quantities have the same direction as the electric field of the cell.

The total current flowing through the cross-section of the  $k$ -th ( $k = 0$  at the apex) slice is cumulative from the apex to the base as dictated by the continuity equation, i.e

$$I_k = I_{k-1} + \sum_{c \in S_k} i_c \quad (9)$$

where  $S_k$  denotes the surface cells of the  $k$ -th slice. The total heat deposited on the  $k$ -th slice is the sum of the Joule and the Nottingham heat components, i.e

$$P_k = \rho_k \frac{I_k^2}{A_k} \Delta z + \sum_{c \in S_k} p_{N_c}. \quad (10)$$

The Euler scheme for equation (8) is  $T_k(t + \Delta t) = T_k(t) + \Delta T_k$ . Using equation (10) yields

$$\Delta T_k = \frac{\Delta t}{C_V A_k \Delta z} \left[ \frac{\kappa_k A_k}{\Delta z} (T_{k+1} + T_{k-1} - 2T_k) + \frac{1}{4\Delta z} (A_{k+1} \kappa_{k+1} - A_{k-1} \kappa_{k-1}) (T_{k+1} - T_{k-1}) + P_k \right] \quad (11)$$

where the subscript denotes the slice number for all quantities. Equation (11) is solved numerically for all slices with a Dirichlet boundary condition at the bottom of the tip, i.e  $T_N = 300$ K and a Neumann condition at the apex, i.e  $T_{-1} = T_0$ .  $\rho_k$  and  $\kappa_k$  are updated at each time step according to the current  $T_k$ . On the other hand,  $A_k$  and  $P_k$  are recalculated and updated when either the field distribution is recalculated by FEMOCS (meaning that the atoms have been displaced more than a limit) or  $T(z)$  has an RMS difference greater than 1% compared to the last step when  $A_k$  and  $P_k$  were obtained.

Finally, the resulting temperature distribution  $T(z)$  is used to control the temperature of the MD system. The velocities of the atoms residing inside the  $k$ -th slice are scaled according to a Berendsen control scheme<sup>47</sup> with control temperature  $T_k$  and relaxation time  $\tau = 1.5$ ps. This  $\tau$  is much smaller than the relaxation time of the heat equation, but also big enough to avoid artefacts appearing in MD when intense velocity scaling.

The above 1D model has the advantage of its simplicity and computational efficiency. Solving the heat equation in 1D adds insignificant CPU time in the whole MD and field calculation. In order to validate the model, we compare its results with our previous 3D Finite Element Method (FEM) model<sup>27</sup>. That model is used to solve the steady-state heat equation on the same FEM mesh produced by FEMOCS. The emitted current and Nottingham heat are in that case calculated using the standard General Thermal-Field (GTF)<sup>31</sup>. Only for this comparison, we will ignore the nanometric emitter size effects in electron emission and the space charge effect. Note that originally the FEM model ignored the Nottingham effect. Nevertheless, it was here implemented by adding a Neumann boundary condition to the heat equation, similar to equation (4) of reference<sup>27</sup>. The boundary condition is

$$\hat{n} \cdot (\kappa \nabla T) = p_N \quad (12)$$

where  $p_N$  denotes the surface density of the deposited heating power and  $\hat{n}$  is the unit vector normal to the material surface.

Figure 5 shows the comparison between the two models. The lines correspond to the final steady-state (after about 100ps) temperature distribution along the simulated tip, as calculated with the 1D model described above. The markers correspond to the temperature along the vertical axis of symmetry of the tip, as calculated by the 3D FEM model. The calculation was performed for two different tip geometries, taken from two different

frames of the simulation shown in the main text. The calculation for a "regular tip" (solid lines and dots) corresponds to the original regular conical geometry (shown in figure 1a,b in the main text) and the one for "deformed tip" (dashed lines and diamonds) to the deformed shape the tip takes after 208.6ps of simulation (see figure 2 of the main text). We see that the simplified 1D model is in excellent agreement with the 3D FEM calculation, even for the irregular geometry of the "deformed tip". The markers correspond to the mean value of the temperature for a given slice. The deviation of the temperature around that value is smaller than the size of the marker in the figure.

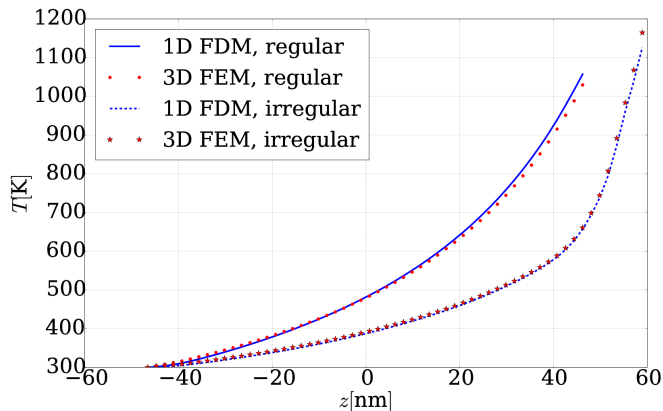


FIG. 5. Steady state temperature distribution as calculated by the 1D FDM (blue lines) and the 3D FEM (red lines) models for two different tip geometries and field values. For the regular conical geometry "Tip 1" (solid lines) the applied field was  $E_{appl} = 0.56\text{GV/m}$  and for the oblique geometry "Tip 2" (dashed lines)  $E_{appl} = 0.45\text{GV/m}$ .

\* andreas.kyritsakis@helsinki.fi; akyritys1@gmail.com

<sup>1</sup> W. Dyke and J. Trolan, *Physical Review* **89**, 799 (1953).

<sup>2</sup> W. Dyke, J. Trolan, E. Martin, and J. Barbour, *Physical Review* **91**, 1043 (1953).

<sup>3</sup> W. Dolan, W. Dyke, and J. Trolan, *Physical Review* **91**, 1054 (1953).

<sup>4</sup> W. Hartmann and M. A. Gundersen, *Phys. Rev. Lett.* **60**, 2371 (1988).

<sup>5</sup> A. Anders, S. Anders, and M. A. Gundersen, *Phys. Rev. Lett.* **71**, 364 (1993).

<sup>6</sup> R. V. Latham, *High voltage vacuum insulation: Basic concepts and technological practice* (Elsevier, 1995).

<sup>7</sup> A. Anders, *Cathodic Arcs*, 1st ed., Vol. 3 (Springer-Verlag New York, 2008).

<sup>8</sup> A. Descoeur, Y. Levinsen, S. Calatroni, M. Taborrelli, and W. Wuensch, *Physical Review Special Topics - Accelerators and Beams* **12** (2009), 10.1103/PhysRevSTAB.12.092001.

<sup>9</sup> I. G. Brown, J. E. Galvin, and R. A. MacGill, *Applied Physics Letters* **47**, 358 (1985).

<sup>10</sup> G. McCracken, *Journal of Nuclear Materials* **93 94** Oct,

3 (1980).

<sup>11</sup> P. Slade, *The Vacuum Interrupter: Theory, Design, and Application* (CRC Press, 2007).

<sup>12</sup> M. Aicheler, P. Burrows, M. Draper, T. Garvey, P. Lebrun, K. Peach, N. Phinney, H. Schmickler, D. Schulte, and N. Tog, eds., *A Multi-TeV linear collider based on CLIC technology: CLIC Conceptual Design Report* (CERN, 2012).

<sup>13</sup> G. A. Mesyats, *IEEE Transactions on Plasma Science* **23**, 879 (1995).

<sup>14</sup> G. Mesyats, *JETP LETTERS* **57**, 95 (1993).

<sup>15</sup> G. A. Mesyats, *Plasma Physics and Controlled Fusion* **47**, A109 (2005).

<sup>16</sup> V. Krohn and G. Ringo, *Applied Physics Letters* **27**, 479 (1975).

<sup>17</sup> A. Wagner, *Applied Physics Letters* **40**, 440 (1982), cited By 36.

<sup>18</sup> L. Swanson, *Nuclear Instruments and Methods in Physics Research* **218**, 347 (1983).

<sup>19</sup> H. Timko, K. Ness Sjobak, L. Mether, S. Calatroni, F. Djurabekova, K. Matyash, K. Nordlund, R. Schneider,

- and W. Wuensch, *Contributions to Plasma Physics* **55**, 299 (2015).
- <sup>20</sup> H. Timko, K. Ness Sjobak, L. Mether, S. Calatroni, F. Djurabekova, K. Matyash, K. Nordlund, R. Schneider, and W. Wuensch, *Contributions to Plasma Physics* **55**, 299 (2015).
- <sup>21</sup> W. B. Nottingham, *Phys. Rev.* **49**, 78 (1936).
- <sup>22</sup> F. M. Charbonnier, R. W. Strayer, L. W. Swanson, and E. E. Martin, *Phys. Rev. Lett.* **13**, 397 (1964).
- <sup>23</sup> F. Djurabekova, S. Parviainen, A. Pohjonen, and K. Nordlund, *Physical Review E - Statistical, Nonlinear, and Soft Matter Physics* **83** (2011), 10.1103/PhysRevE.83.026704.
- <sup>24</sup> M. Veske, A. Kyritsakis, F. Djurabekova, R. Aare, K. Eimre, and V. Zadin, in *2016 29th International Vacuum Nanoelectronics Conference (IVNC)* (2016) pp. 1–2.
- <sup>25</sup> M. Veske, A. Kyritsakis, K. Eimre, V. Zadin, A. Aabloo, and F. Djurabekova, *ArXiv e-prints* (2017), arXiv:1706.09661.
- <sup>26</sup> S. Parviainen, F. Djurabekova, H. Timko, and K. Nordlund, *Computational Materials Science* **50**, 2075 (2011).
- <sup>27</sup> K. Eimre, S. Parviainen, A. Aabloo, F. Djurabekova, and V. Zadin, *Journal of Applied Physics* **118** (2015), 10.1063/1.4926490.
- <sup>28</sup> W. Schottky, *Zeitschrift für Physik* **14**, 63 (1923).
- <sup>29</sup> R. H. Fowler and L. Nordheim, *Proceedings of the Royal Society of London A: Mathematical, Physical and Engineering Sciences* **119**, 173 (1928).
- <sup>30</sup> E. L. Murphy and R. H. Good, *Phys. Rev.* **102**, 1464 (1956).
- <sup>31</sup> K. L. Jensen and M. Cahay, *Applied Physics Letters* **88** (2006), 10.1063/1.2193776.
- <sup>32</sup> J. He, P. Cutler, and N. Miskovsky, *Applied Physics Letters* **59**, 1644 (1991).
- <sup>33</sup> A. Kyritsakis and J. P. Xanthakis, *Proceedings of the Royal Society A: Mathematical, Physical and Engineering Sciences* **471** (2015), 10.1098/rspa.2014.0811.
- <sup>34</sup> A. Kyritsakis and J. Xanthakis, *Journal of Applied Physics* **119** (2016), 10.1063/1.4940721.
- <sup>35</sup> A. Kyritsakis and F. Djurabekova, *Computational Materials Science* **128**, 15 (2017).
- <sup>36</sup> C. D. Child, *Phys. Rev. (Series I)* **32**, 492 (1911).
- <sup>37</sup> K. L. Jensen, in *Wiley Encyclopedia of Electrical and Electronics Engineering* (John Wiley & Sons Inc., 1999).
- <sup>38</sup> P. Chen, T. Cheng, J. Tsai, and Y. Shao, *Nanotechnology* **20**, 405202 (2009).
- <sup>39</sup> I. V. Uimanov, *IEEE Transactions on Dielectrics and Electrical Insulation* **18**, 924 (2011).
- <sup>40</sup> R. G. Forbes, *Journal of Applied Physics* **104**, 084303 (2008).
- <sup>41</sup> J. Barbour, W. Dolan, J. Trolan, E. Martin, and W. Dyke, *Physical Review* **92**, 45 (1953).
- <sup>42</sup> R. A. Matula, *Journal of Physical and Chemical Reference Data* **8**, 1147 (1979).
- <sup>43</sup> G. R. Gathers, *International Journal of Thermophysics* **4**, 209 (1983).
- <sup>44</sup> A. E. Yarimbiyik, H. A. Schafft, R. A. Allen, M. E. Zaghloul, and D. L. Blackburn, *Microelectronics Reliability* **46**, 1050 (2006).
- <sup>45</sup> A. Bejan and A. D. Kraus, *Heat transfer handbook*, Vol. 1 (John Wiley & Sons, 2003).
- <sup>46</sup> P. Nath and K. Chopra, *Thin Solid Films* **20**, 53 (1974).
- <sup>47</sup> H. J. C. Berendsen, J. P. M. Postma, W. F. van Gunsteren, A. DiNola, and J. R. Haak, *The Journal of Chemical Physics* **81**, 3684 (1984).
- <sup>48</sup> M. J. Sabochick and N. Q. Lam, *Phys. Rev. B* **43**, 5243 (1991).
- <sup>49</sup> Y. Mishin, M. J. Mehl, D. A. Papaconstantopoulos, A. F. Voter, and J. D. Kress, *Phys. Rev. B* **63**, 224106 (2001).
- <sup>50</sup> M. Ester, H.-P. Kriegel, J. Sander, X. Xu, *et al.*, in *Kdd*, Vol. 96 (1996) pp. 226–231.
- <sup>51</sup> M. Kildemo, *Nuclear Instruments and Methods in Physics Research, Section A: Accelerators, Spectrometers, Detectors and Associated Equipment* **530**, 596 (2004).